

PROBING THE REIONIZATION HISTORY USING THE SPECTRA OF HIGH-REDSHIFT SOURCES

ANDREI MESINGER, ZOLTÁN HAIMAN

Department of Astronomy, Columbia University, 550 West 120th Street, New York, NY 10027

AND

RENYUE CEN

Department of Astrophysical Sciences, Princeton University, Peyton Hall, Ivy Lane, Princeton, NJ 08544

To appear in ApJ, vol. 613, 20 September 2004

ABSTRACT

We quantify and discuss the footprints of neutral hydrogen in the intergalactic medium (IGM) on the spectra of high-redshift ($z \sim 6$) sources, using mock spectra generated from hydrodynamical simulations of the IGM. We show that it should be possible to extract relevant parameters, including the mean neutral fraction in the IGM, and the radius of the local cosmological Strömgren region, from the flux distribution in the observed spectra of distant sources. We focus on quasars, but a similar analysis is applicable to galaxies and gamma ray burst (GRB) afterglows. We explicitly include uncertainties in the spectral shape of the assumed source template near the Lyman α line. Our results suggest that a mean neutral hydrogen fraction, x_H of unity can be statistically distinguished from $x_H \sim 10^{-2}$, by combining the spectra of tens of bright ($M \sim -27$) quasars. Alternatively, the same distinction can be achieved using the spectra of several hundred sources that are ~ 100 times fainter. Furthermore, if the radius of the Strömgren sphere can be independently constrained to within $\sim 10\%$, this distinction can be achieved using a single source. The information derived from such spectra will help in settling the current debate as to what extent the universe was reionized at redshifts near $z \sim 6$.

1. INTRODUCTION

The epoch of cosmological reionization is a significant milestone in the history of structure formation. Despite recent observational breakthroughs, the details of the reionization history remain poorly determined. The Sloan Digital Sky Survey (SDSS) has detected large regions with no observable flux in the spectra of several $z \sim 6$ quasars (Becker et al. 2001; Fan et al. 2003; White et al. 2003). The presence of these Gunn-Peterson (GP) troughs set a lower limit on the volume weighted hydrogen neutral fraction of $x_H \sim 10^{-3}$ (Fan et al. 2002). This strong limit implies a rapid evolution in the ionizing background from $z = 5.5$ to $z \sim 6$ (Cen & McDonald 2002; Fan et al. 2002; Lidz et al. 2002; Pentericci et al. 2002), and suggests that we are witnessing the end of the reionization epoch, with the IGM becoming close to fully neutral at $z \sim 7$ (but see Songaila & Cowie 2002 for a different conclusion). On the other hand, recent results from the Wilkinson Microwave Anisotropy Probe (WMAP) have uncovered evidence for a large optical depth to electron scattering, $\tau \sim 0.17 \pm 0.04$ (Bennett 2003) in the cosmic microwave background anisotropies. Assuming a step-function model for the reionization history, this result would indicate that reionization began at $z \sim 17 \pm 4$ (Kogut et al. 2003; Spergel et al. 2003). Although physically motivated “double” reionization scenarios, proposed prior to the WMAP result (Cen 2003a; Wyithe & Loeb 2003) are consistent with the combined observations, the details of the reionization process remain far from being clear.

Numerous recent theoretical works have addressed resolutions of the apparent discrepancy (see, e.g., Haiman 2003 for a review). Successful models incorporate various feedback effects, such as that due to metal-enrichment (Cen 2003b; Wyithe & Loeb 2003) or associated with the UV radiation produced by the early ionizing sources (Haiman & Holder 2003). Alternatively, the high-redshift “tail” of ionization has been attributed to an early population of X-ray producing black holes (Ricotti

& Ostriker 2003; Madau et al. 2003) or even to something more exotic, such as decaying particles (Hansen & Haiman 2003). These competing reionization scenarios each predict a different evolution of the neutral fraction beyond $z \sim 6$. It would therefore be quite beneficial to observationally determine the values of x_H at the intermediate redshifts of $6 < z < 30$.

As a first step towards this goal, differentiating between a neutral and a mostly ionized universe at redshifts just beyond $z \sim 6$, would already aid in discriminating between several models (Haiman & Holder 2003). To do this however, one requires a more detailed statistic than the presence or absence of a Gunn-Peterson trough. In this paper, we utilize the transmitted flux distribution of a hypothetical $z \sim 6$ source near its Ly α wavelength. While most of the flux on the blue side of Ly α is simply extinguished for a wide range of neutral fractions ($10^{-3} < x_H < 1$), detectable flux can be transmitted close to the line center, at wavelengths corresponding to a local HII region around the source (e.g. Cen & Haiman 2000; Madau & Rees 2000). The spectrum on the blue side, as well as the flux processed by the damping wing of IGM absorption and transmitted on the red side of the Ly α line (Miralda-Escudé 1998), depends on the hydrogen neutral fraction of the IGM in which the source is embedded. As a result, the flux distributions can be used as a probe of the neutral fraction in the IGM.

There are two immediate apparent difficulties with the above approach. First, it requires an estimate of the intrinsic spectrum of the source. Second, it requires an ab-initio model of the density (and velocity) fields surrounding the source, which will influence the transmitted flux distribution. Since both of these quantities are impossible to predict accurately from first principles for any specific source and line of sight, a single spectrum is unlikely to provide tight constraints on the neutral fraction. However, the hydrogen neutral fraction can still be inferred statistically, by studying the spectra of a sample of sources. *The purpose of this paper is to quantify the accuracy to which x_H can be determined in a future sample of high redshift sources,*

taking the above complications into account. We use a hydrodynamical simulation to generate mock spectra of sources for different assumed values of the hydrogen neutral fraction of the IGM, and quantify the statistical confidence to which these transmitted spectra can be distinguished from each other.

The rest of this paper is organized as follows. In § 2, we discuss the basic signatures of neutral hydrogen in the IGM that should be imprinted on the spectrum of a background source. In § 3, we describe the method we use to produce mock spectra. In § 4, we present the statistical comparison between the various mock spectra, and assess the accuracy with which the input neutral fraction can be recovered in each case. In § 5, we discuss the relative merits of using different source types (quasars, galaxies or gamma ray burst afterglows), and some related issues. In § 6, we explore the benefits of independently constraining the radius of the Strömgen sphere. Finally, we summarize the implications of this work and offer our conclusions in § 7.

We use redshift, z , and the observed wavelength, λ_{obs} , interchangeably throughout this paper as a measure of the distance away from the source along the line of sight. These can be related by: $(1+z) = \lambda_{\text{obs}} / \lambda_{\text{rest}}$, where $\lambda_{\text{rest}} = 1215.67 \text{ \AA}$ is the rest-frame wavelength of the Ly α line center. The proper distance from a source at redshift z_s to a point at redshift z , is determined by $r = \int_{z_s}^z dz' c \frac{dt}{dz'}$, where $c(dt=dz')$ is the line element in a given cosmology, and the comoving distance is $(1+z)$ times the proper distance. For reference, in our case a proper distance of 6 Mpc corresponds to about $\lambda_{\text{obs}} = 100 \text{ \AA}$.

Throughout this paper, we assume a standard Λ CDM cosmology, with $(\Omega_m; \Omega_b; n; \sigma_8; H_0) = (0.71, 0.29, 0.047, 1, 0.85, 70 \text{ km/s/Mpc})$, consistent with the recent results from WMAP (Spergel et al. 2003). Unless stated otherwise, all lengths are quoted in comoving units.

2. SPECTRAL SIGNATURES OF NEUTRAL HYDROGEN

In this section, we summarize the spectral signatures of neutral hydrogen in the IGM. The spectrum emitted by a source at redshift z_s , $F_0(\lambda)$, will be modified around the Ly α wavelength by absorption by neutral hydrogen atoms along the line of sight, so that we observe $F(\lambda) = F_0(\lambda) \exp(-\tau(\lambda; z_s))$. The total optical depth due to Ly α absorption, τ , between an observer at $z = 0$ and a source at $z = z_s$, at an observed wavelength of $\lambda_{\text{obs}} = \lambda_s(1+z_s)$, is given by:

$$\tau_{\text{Ly}\alpha}(\lambda_{\text{obs}}) = \int_0^{z_s} dz c \frac{dt}{dz} n_H(z) x_H(z) \frac{\sigma_{\text{Ly}\alpha}^{\text{obs}}}{1+z} \quad (1)$$

where $c(dt=dz)$ is the line element in a given cosmology, $n_H(z)$ is the hydrogen number density at redshift z , $x_H(z)$ is the hydrogen neutral fraction at redshift z , and $\sigma_{\text{Ly}\alpha}^{\text{obs}}$ is the Ly α absorption cross section. Since high-redshift sources sit in their own highly ionized Strömgen spheres¹, the total optical depth at a given λ_{obs} can be written as the sum of contributions from inside and outside the Strömgen sphere, $\tau = \tau_R + \tau_D$. The resonant optical depth, τ_R , is given by:

$$\tau_R(\lambda_{\text{obs}}) = \int_{z_{\text{HII}}}^{z_s} dz c \frac{dt}{dz} n_H(z) x_H(z) \frac{\sigma_{\text{Ly}\alpha}^{\text{obs}}}{1+z} \quad (2)$$

¹The assumption of discrete HII regions is invalid if hard spectra dominate reionization. In this case, the surface of the HII region can have a width that exceeds the separation between the ionizing sources (Oh 2001; Venkatesan et al. 2001). There is still a proximity region around each source, within which they dominate the cosmic background, which could be used in the analysis below in place of the Strömgen sphere.

and the damping wing optical depth for the IGM outside the Strömgen sphere can be obtained from

$$\tau_D(\lambda_{\text{obs}}) = \int_{z_{\text{end}}}^{z_{\text{HII}}} dz c \frac{dt}{dz} n_H(z) x_H(z) \frac{\sigma_{\text{Ly}\alpha}^{\text{obs}}}{1+z} \quad (3)$$

where z_{HII} corresponds to the redshift of the edge of the Strömgen sphere, and z_{end} denotes the redshift by which HI absorption is insignificant along the line of sight to the source. For a smooth IGM, we would simply have $n_H(z) = n_{\text{H}\alpha} (1+z)^3$, and since the fall-off of the cross section is rapid compared to the change in $x_H(z)$, we can also approximate $x_H \approx \text{constant}$, for the smooth IGM in eq. (3). Conversely, the fall-off of the cross section is slow compared to the small-scale fluctuations in the IGM, averaging out their contributions to τ_D . For these reasons, in this paper we approximate $x_H \approx \text{constant}$, and assume a smooth IGM. The value of z_{end} was chosen to be $z_{\text{end}} = z_{\text{HII}} - 0.5$. As long as we are not looking through another source's Strömgen sphere close to z_{HII} , we find that the exact value of z_{end} is irrelevant because most of the contribution to τ_D comes from within $z < 0.5$ of z_{HII} . In particular, a choice of $z_{\text{end}} = z_{\text{HII}} - 0.25$ results in an average change in τ_D of only 4% compared to our fiducial model with $z_{\text{end}} = z_{\text{HII}} - 0.5$. The difference between equations (2) and (3) are: (1) the limits of integration, (2) the determination of x_H , which assumes ionization equilibrium with the cosmological background flux J_{BG} outside the Strömgen sphere with the approximation of $x_H \approx \text{constant}$, and equilibrium with the sum of the background and the local source fluxes, $J_{\text{BG}} + J_s$ inside the HII region with a fluctuating $x_H(z)$, and (3) at the relevant wavelengths where τ_R is significant, the integral in equation (2) is dominated by the resonant cross-sections, whereas at all wavelengths where flux is transmitted, the damping wing dominates equation (3). As a result of this last property, τ_R fluctuates strongly with wavelength, reflecting the local density field, whereas the damping wing contribution is smooth, since it averages the contributions to the damping wing from a relatively wide redshift interval.

The two optical depths are represented in Figure 1 for the case of a bright quasar embedded in a neutral IGM at $z_s = 6$. The opacities were obtained from a simulation (described below) for a typical line of sight towards a source residing at a cosmological density peak. Also shown is R_s , the radius of the Strömgen sphere, corresponding to the region of transmitted flux blueward of the Ly α line center. It is worthwhile to note that there are different wavelength regions where either the resonant or the damping wing absorption dominates. These regions can shift according to the epoch being studied, since τ_D scales linearly with x_H , and also according to the quasar's luminosity L , since $\tau_R \propto L^{-1}$ (see eq. [4]). For example, since the damping wing is less dominant close to the line center for lower x_H , details of the gas density and velocity distribution can be studied in this regime. Shortward of the edge of the Strömgen sphere, no flux is observed for $10^{-3} < x_H < 1$, since the attenuation is large (ranging from $e^{-10^6} - e^{-10^3}$ for the values of the neutral fraction studied in this paper).

Simple modeling predicts several distinctive signatures that x_H should leave on a spectrum (see also Fig. 2 and accompanying discussion below). Most importantly: on average, a neutral universe would be expected to have a smoother spectrum on the blue side of the line, due to the larger contribution to the total optical depth from the IGM, which is a smooth function (see Fig. 1).

In addition, the *symmetry* of the observed spectrum around

the Ly α line center should be affected by x_H . Since $R \neq 0$ on the red side of the Ly α line, the observed spectrum should trace out the emitted spectrum for low values of x_H . For low values of x_H , the red side of the line has negligible absorption, while the blue side is still affected by resonance absorption. This makes the observed spectrum highly asymmetric. In comparison, in a neutral universe, the presence of a strong damping wing (D) causes additional strong suppression on the red side of the line, as well, making the line more symmetric (though overall weaker). Note that if we were to model out R , leaving only the damping wing contributing to optical depth, a neutral universe would have a more asymmetric spectrum, because the damping wing would impose a sharper slope in the transmitted spectrum near the Ly α line. Furthermore, in a composite spectrum, one expects there to be a sharp drop in observed flux at the edge of the Strömgen sphere if the universe is mostly ionized. This occurs since the gradual cusp of the damping wing (immediately longward of the sharp rise in D , c.f. Fig. 1), is sub-dominant if the universe is mostly ionized, making the transition from resonance-dominated to damping wing-dominated optical depth more sudden (see feature at 8390 Å, in the lower panel of Fig. 3). On the other hand, if the universe is neutral, the damping wing cusp dominates at the edge of the Strömgen sphere, and creates a gradual drop-off in the observed flux (see the upper panel of Fig. 3). This effect is only observable if the Strömgen sphere is not large enough that R , whose mean value scales as the square of the distance from the source, blocks off the observed spectrum by itself.

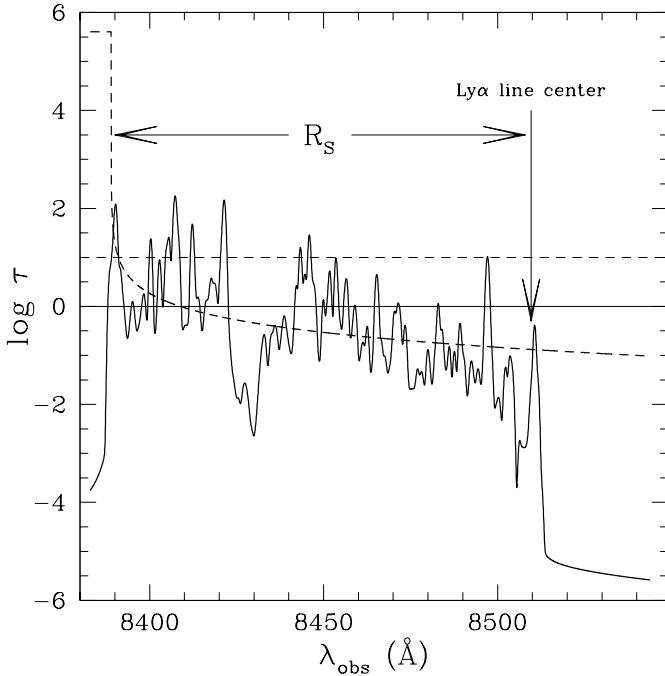


FIG. 1.— Optical depth contributions from within (R) and from outside (D) the local HII region for a typical line of sight towards a $z_s = 6$ quasar embedded in a fully neutral IGM. The dashed line corresponds to D , and the solid line corresponds to R . For details concerning the simulation, see § 3. In this example, the damping wing of the IGM, D , contributes significantly to the total optical depth at $\lambda_{\text{obs}} = 8430$ Å and $\lambda_{\text{obs}} = 8470$ Å.

The above effects manifest themselves in all high-redshift sources (quasars, galaxies, GRB afterglows), and furthermore, they also scale predictably with the source strength and envi-

ronment.² As we will see below, the effects are difficult to detect or quantify for a single high-redshift spectrum, due to the uncertainty in the shape of the source's intrinsic emission, and to the stochastic nature of the density field along a given line of sight. However, with many sources such statistics can be usefully analyzed.

3. SIMULATION OF SPECTRA

We use a Λ CDM hydrodynamical simulation box at redshift $z_s = 6$ as the home of our source quasar. The simulations are described in detail in (Cen et al. 2004), and we only briefly summarize the relevant parameters here. The box is $11 h^{-1}$ Mpc on each side, with each pixel being about $25.5 h^{-1}$ kpc. This scale resolves the Jeans length in the smooth IGM by more than a factor of 10. The simulation also includes feedback in the form of realistic galactic winds. Stellar particles are treated dynamically as collisionless particles, except that feedback from star formation is allowed in three forms: UV ionizing field, supernova kinetic energy, and metal rich gas, all being proportional to the local star formation rate. Supernova energy and metals from aging massive stars are ejected into the local gas cells where stellar particles are located. Supernova energy feedback into the IGM is included with an adjustable efficiency (in terms of rest-mass energy of total formed stars) of e_{SN} , which is normalized to observations (Cen et al. 2004, in preparation).

We first identified the densest region in the box, as the natural location of a high-redshift source, such as a quasar. This corresponds to a pixel with an overdensity of $n = n_i \approx 10^4$ relative to the background, and to the center of a collapsed dark matter halo with mass, $M_{\text{halo}} \approx 2 \times 10^9 M_\odot$. Density and velocity information was then extracted from 92 different lines of sight (LOSs), approximately evenly spaced in solid angle, originating from this pixel. The step size along each line of sight (LOS) was taken to be $5.1 h^{-1}$ kpc, which resolves the Ly α Doppler width by more than a factor of 40. The exact value of the step size was chosen somewhat arbitrarily, and does not influence the results as long as it adequately resolves the Doppler width. At each step, the density and velocity values were averaged for the neighboring pixels, and weighted by the distance to the center of the pixels. We extended each LOS by the common practice of randomly choosing a LOS through the box, and stacking the pieces together (Cen et al. 1994).

The hydrogen neutral fraction inside the Strömgen sphere, $x_H(z)$, was calculated at each step in the LOS, and for several values of an isotropic background flux, $J_{\text{BG}}(\lambda)$ (in units of $\text{erg s}^{-1} \text{cm}^{-2} \text{Hz}^{-1} \text{sr}^{-1}$), corresponding to a particular x_H . Assuming ionization equilibrium, and $x_H(z) = 1$ inside the Strömgen sphere:

$$x_H(z) = \frac{n_H}{n_H + \frac{J_{\text{BG}}(\lambda)}{4\pi r^2} \frac{B}{h\nu}} \quad (4)$$

where ν_H and σ_H are the ionization frequency and cross section of hydrogen, respectively, B is the hydrogen recombination coefficient at $T = 15,000$ K, r is the luminosity distance between the source and redshift z , and L is the quasar's intrinsic luminosity in $\text{erg s}^{-1} \text{Hz}^{-1}$. The luminosity was taken to be $L = 2.34 \times 10^{31} (\nu_H)^{-1.8} [(1+z)/(1+z_s)]^{-0.8}$, which results from redshifting a power-law spectrum with a slope of -1.8 , nor-

²Spectra of GRB afterglows originating in high redshift galaxies might not have noticeable R , since the host galaxies could be too young or too faint to produce a significant Strömgen sphere (Barkana & Loeb 2004, Lamb & Haiman 2003).

malized such that the emission rate of ionizing photons per second is 2×10^7 , matching the Elvis et al. (1994) template spectrum and the brightness typical of the SDSS quasars. The background flux, $J_{BG}(\lambda)$, is also assumed to follow a $\lambda^{-1.8}$ power-law spectrum. Results are insensitive to the shape of the background flux, since the dominant effect of $J_{BG}(\lambda)$ comes from the damping wing, and that only depends on the value of x_H . Since the quasar's luminosity is dominant for the values of interest inside the Strömgen sphere, we find that equation (4) can be very well approximated by $x_H(z) = 4 \times 10^{-9} n_H(z) B^1(z) (L = h) d$.

For several combinations of z_{HII} (corresponding to a Strömgen sphere radius, R_S) and x_H , the integrals in (2) and (3) were evaluated for each LOS. To expedite analysis, D was also calculated using the approximation (Miralda-Escudé 1998):

$$D = 6.43 \times 10^9 x_H \frac{e^2 f n_H(z)}{m_e c H(z)} \quad (5)$$

$$I = \frac{1+z_{\text{HII}}}{1+z} - I \frac{1+z_{\text{end}}}{1+z}$$

where:

$$I(x) = \frac{x^{9/2}}{1-x} + \frac{9}{7}x^{7/2} + \frac{9}{5}x^{5/2} + 3x^{3/2} + 9x^{1/2}$$

$$- \ln \frac{1+x^{1/2}}{1-x^{1/2}}$$

Equations (3) and (5) give very similar results for wavelengths away from resonance (i.e. inside the Strömgen sphere), but (5) is much quicker to compute.

The Voigt profile was used to approximate the Ly α absorption cross section (Rybicki & Lightman 1979). We assumed a temperature of 15,000 K for gas inside the Strömgen sphere. Outside the Strömgen sphere, for the case of a mostly ionized universe, an IGM temperature of $T = 10^4$ K was used, while the temperature in a neutral universe was taken to be $T = 2.73 \times 151 \left(\frac{1+z}{151}\right)^2$ K, valid for $z < 150$ (Peebles 1993). Our results are insensitive to the exact temperature used. The Doppler width of the Ly α absorption cross section scales as $D / T^{1/2}$, but the total integrated area under the cross section is independent of temperature.

Finally, to simulate observations, we had to smooth the raw spectra we compute. Physical smoothing due to gas pressure, present in the simulations on scales of ~ 10 km/s (Gnedin 2000) corresponds to smoothing on a wavelength range of $\lambda_{\text{obs}} = \lambda_s(1+z_s)$, or ~ 0.3 Å at $z_s = 6$. However, current spectral resolutions achieved for high-redshift quasars (APO, Keck) are about a factor of three worse than this value. In order to simulate a realistic spectral resolution of ~ 1 Å, all resulting spectra were smoothed over 1 Å bins (20 steps in a LOS) by averaging e^- over each bin.

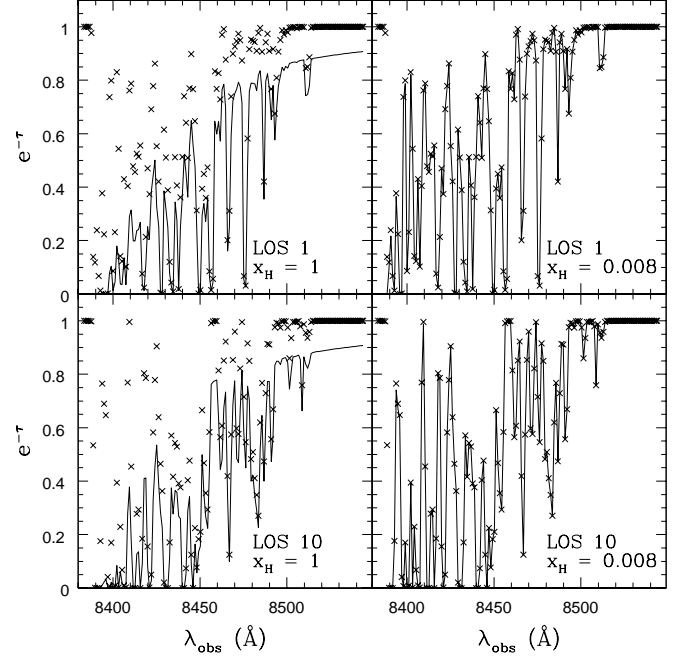


FIG. 2.— Simulated e^- for two different LOSs (top and bottom) in two different x_H regimes: $x_H = 1$ (left panels) and $x_H = 0.008$ (right panels). All spectra correspond to $R_S = 43$ Mpc. The solid line corresponds to e^- from equation (1) and the discrete points correspond to e^- from equation (2). The sharp absorption features in the figures are produced by R , while the general trend of increasing optical depth away from the line center is a combination of both R and D .

4. INTERPRETATION OF SPECTRA

For illustrative purposes, in Figure 2 we show four different examples for the spectrum of a source with $R_S = 43$ Mpc. We show spectra assuming two different values of x_H : 1 or 0.008, corresponding to $J_{BG}(\lambda_H) = 0$ and 8×10^{-25} erg s $^{-1}$ cm $^{-2}$ Hz $^{-1}$ sr $^{-1}$, respectively. This range for the background flux is approximately what is allowed by the current analysis of known $z \sim 6$ quasars (e.g. Fan et al. 2003; Cen & McDonald 2002). The value of R_S was chosen because it is representative of the brightest SDSS quasars, and it corresponds to the radius of a sphere enclosing 2×10^7 ionizing photons per second 10^5 s hydrogen atoms (Cen & Haiman 2000b). The value of the source's Strömgen sphere radius is left as a free parameter to be determined by the inversion method (described below).

Also, shown in Figure 2 is the effect of the damping wing in smoothing out the spectrum. The flux decrement due to resonance absorption, $e^- R$, is shown with discrete points, and the total flux decrement, $e^- R - D$, is represented with a solid line for two different LOSs (top and bottom). Flux decrements from a neutral universe (left panels) are visibly smoother than those of a mostly-ionized universe (right panels), as predicted. The sharp absorption features in the figures are produced by R , while the general trend of increasing optical depth away from the line center is a combination of both R and D .

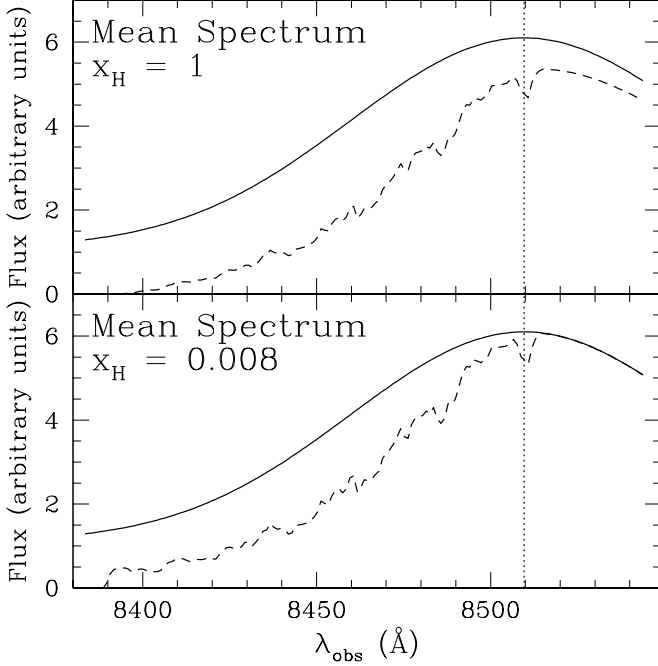


FIG. 3.— Composite mean spectra from 92 LOSs, for the cases of $x_H = 1$ (top panel) and $x_H = 0.008$ (bottom panel). For illustrative purposes, a Gaussian + continuum emission template is overlaid (solid line), and the resulting mean observed spectrum is shown underneath (dashed line). The source quasar is at redshift, $z_s = 6$, and the Ly α line center is at 8509.69 Å (dotted line). The spectrum shown in the top panel is measurably smoother than the one shown in the bottom panel.

In Figure 3, we show the composite mean spectra from 92 LOSs, for the two different values of x_H : 1 (top panel) and 0.008 (bottom panel). For illustrative purposes, a Gaussian + continuum emission template is overlaid (solid line), and the resulting mean observed spectrum is shown underneath (dashed line). The emission template was chosen somewhat arbitrarily, in order to resemble the typical spectrum of observed quasars (e.g. Vanden Berk et al. 2001), and is comprised of a flat continuum emission added to a Gaussian of width 2500 km/s and a peak-to-continuum ratio of ~ 5 . From Figures 2 and 3, we can see that the composite mean spectra for these regimes exhibit the traits discussed in § 2: spectra from a neutral universe are smoother on the blue side of the line and more symmetric around the line center (at 8509.69 Å); however, if the R contribution is statistically modeled out, the $x_H = 0.008$ spectra would be more symmetric; also there is a sharp drop in the composite observed flux at the edge of the Strömgren sphere in the $x_H = 0.008$ universe, that is not present in the neutral universe composite spectrum. The latter feature is only statistically detectable from a large sample of LOSs, and was not used in our analysis below. In the analysis below, we ignore the ~ 5 Å range redward of the edge of the Strömgren sphere, since in this region, the exact structure of the transition region from the Strömgren sphere to the IGM contributed significantly to D , and the transition region can have a large spectrum-to-spectrum variability.

4.1. Inverting the Observed Spectrum to Find x_H

We are now presented with an interesting problem: supposing the only information we have is the observed spectrum, can we extract the quantities of interest, namely x_H and R_S ? For

the purposes of an idealized analysis, we will first assume that we know the *shape* of the intrinsic emission template to infinite precision (however, we do not assume knowledge of the *amplitude* of the template). In the next section, we shall relax this restriction. The other major assumption we implicitly make is that we can accurately predict the distribution of R , using the small-scale power statistics from the simulation box. This assumption can be checked by studying more extensive simulations in the future (see discussion in § 5 below).

Before diving into the details, we first outline the main steps of the procedure. We start with a simulated observed spectrum. Then we guess values for the radius of the Strömgren sphere, R_S^0 , and the IGM hydrogen neutral fraction, x_H^0 . Next we approximate the amplitude of the source's intrinsic emission, A^0 , implied by the choices of R_S^0 and x_H^0 , using the red side of the Ly α line where resonance absorption can be neglected. From the observed spectrum, we divide out the assumed intrinsic emission (A^0 known spectral shape), and the assumed damping wing flux decrement, $e^{-D(\text{obs}; R_S^0, x_H^0)}$, calling the result $S^0(\text{obs})$. If our choices of R_S^0 and x_H^0 were correct, $S^0(\text{obs})$ should represent the resonance absorption flux decrement alone. Hence, we compare a histogram of the implied resonance optical depths, $-\ln[S^0(\text{obs})]$, to the known histogram of resonance optical depth (obtained from the simulation). We then repeat this procedure with different choices of R_S^0 and x_H^0 , finding the ones whose implied resonance optical depths most closely match the known histogram. We shall now elaborate on this procedure below.

We start with the mock observed flux, of the form:

$$F(\text{obs}) = A e^{-R(\text{obs}) - D(\text{obs}; R_S, x_H)} T(\text{obs}) \quad (6)$$

where A is the amplitude of the adopted normalized emission template $T(\text{obs})$, and $R(\text{obs}) = R(\text{obs}; R_S, x_H)$ also takes into account the small contribution of J_{BG} to $x_H(z)$. Since we assume we know the shape of the source's intrinsic emission, for simplicity we shall set $T(\text{obs}) = 1$. Actual features in the spectrum will only effect the signal-to-noise of detection under this optimistic assumption (see discussion below). Next, we guess values for R_S^0 and x_H^0 . For these values, $D(\text{red}; R_S^0, x_H^0)$ is calculated for a wavelength, λ_{red} , on the red side of the line. We then estimate the amplitude of the intrinsic emission template, which these values would imply at λ_{red} : $A^0 = F(\lambda_{\text{red}}) e^{D(\text{red}; R_S^0, x_H^0)}$. Since for the red side of the line, $R \rightarrow 0$, we are left with the following estimate of the emission amplitude:

$$A^0 = \frac{F(\lambda_{\text{red}})}{e^{D(\text{red}; R_S^0, x_H^0)}} \quad (7)$$

where for increased accuracy, A^0 can be averaged over several values of λ_{red} , corresponding to a smooth region in the red side of the observed spectrum. Since our simulated spectra are well-behaved, averaging was not needed, and A^0 was evaluated at an arbitrarily chosen $\lambda_{\text{red}} = 8514$ Å. It should be noted that, when using real spectra, one has to be careful to choose λ_{red} values that are not near other emission lines.

Next, we divide the input flux by A^0 , and extract an estimate of the resonant optical depth, $\hat{\kappa}(\text{obs})$, using the damping wing contribution, $e^{-D(\text{obs}; R_S^0, x_H^0)}$, for observed wavelengths on the blue side of the line: $\hat{\kappa}(\text{obs}) = -\ln(F(\text{obs}) (A^0)^{-1} e^{D(\text{obs}; R_S^0, x_H^0)})$, which reduces to:

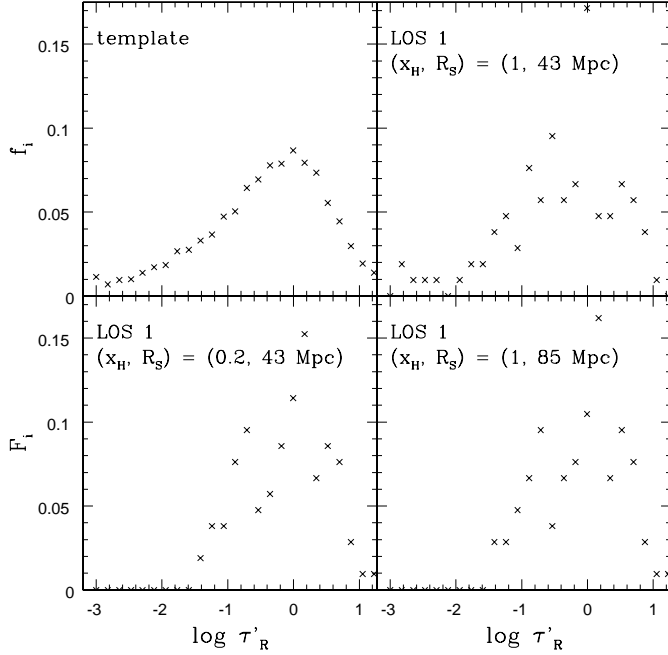


FIG. 4.— Histogram of the template distribution R (top left), and histograms of the derived R distribution: $(x_H; R_S) = (1; 43 \text{ Mpc})$ (top right), $(x_H; R_S) = (0.2; 43 \text{ Mpc})$ (bottom left), $(x_H; R_S) = (1; 85 \text{ Mpc})$ (bottom right). We test the hypothesis that the top right, bottom left and bottom right histograms (among many others in parameter space) were drawn from the distribution in the top left. We find that the top right panel is consistent with being drawn from the distribution in the top left, and that the bottom panels are not.

$$\hat{\chi}_R(\text{obs}) = -\ln(e^{R(\text{obs})} e^{D-D}) - \ln \frac{A}{A^0} \quad (8)$$

where $D = D(\text{obs}; R_S^0; x_H^0)$ and $D = D(\text{obs}; R_S; x_H)$. The first term on the RHS of equation (8) represents our misestimate of the damping wing contribution on the blue side, and the second term represents our misestimate of the continuum inferred from the red side.

Then, a final correction is applied to remove the contribution of the assumed background flux corresponding to our guess of x_H^0, J_{BG}^0 , to the hydrogen neutral fraction inside the Ström-gren sphere, $x_H(z)$, defined by (4):

$$R_R^0(\text{obs}) = \hat{\chi}_R(\text{obs}) \frac{R_1 \left(\frac{L}{4r^2} + 4 \frac{J_{BG}^0}{h} d \right)}{R_1 \left(\frac{L}{4r^2} \right) h d} \quad (9)$$

where $R_R^0(\text{obs})$ is our estimate for the resonance optical depth at obs , for our guess of $(x_H^0; R_S^0)$, and normalized to the resonance optical depth in a neutral universe (i.e. $J_{BG} = 0$ in eq. [4]) for purposes of comparison.

A histogram of R_R^0 is constructed, and compared to the known template histogram of R , extracted from the combined data from 92 smoothed mock spectra, created by embedding the source in a neutral universe (see Figure 4). In order to exclude spectral pixels that would be too faint for an actual flux measurement, the inferred values of $R_R^0 > 16$ were discarded from the analysis. This choice is motivated by the current limits available from the $z \sim 6$ SDSS quasars. The current best lower limit on the optical depth just blueward of the Ly α line is actually worse (~ 6 ; White et al. 2003), but since the higher Lyman series lines have lower opacities, a better lower limit,

22, is available from the Ly β region of the spectrum (White

et al. 2003). In principle, the Ly γ (and Ly δ) spectral regions could be added to our analysis. A χ^2 test statistic is used to compare the two templates:

$$\chi^2 = N_{\text{points}} \sum_{i=1}^{N_{\text{bins}}} \frac{(f_i - F_i)^2}{f_i} \quad (10)$$

where N_{points} is the number of R values extracted from the spectrum, f_i and F_i are the fraction of values expected and received in bin i , respectively. The deviations are approximately Gaussian, $\chi^2 = N_{\text{points}} f_i$.

This procedure is then repeated for many choices of R_S^0 and x_H^0 (shown below), and the χ^2 test statistic in equation (10) is minimized.

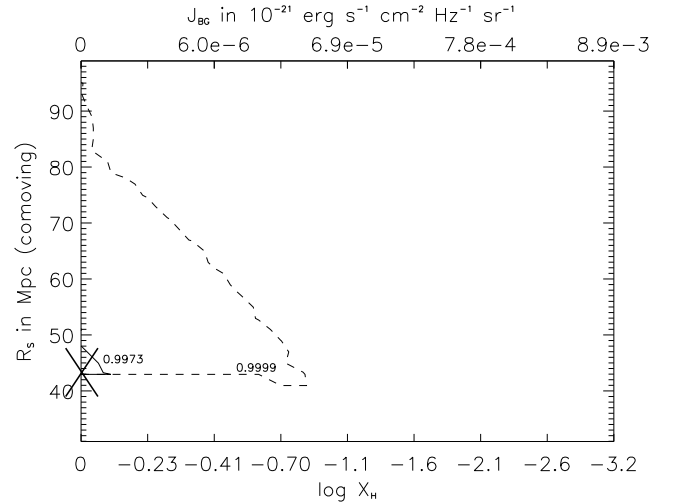
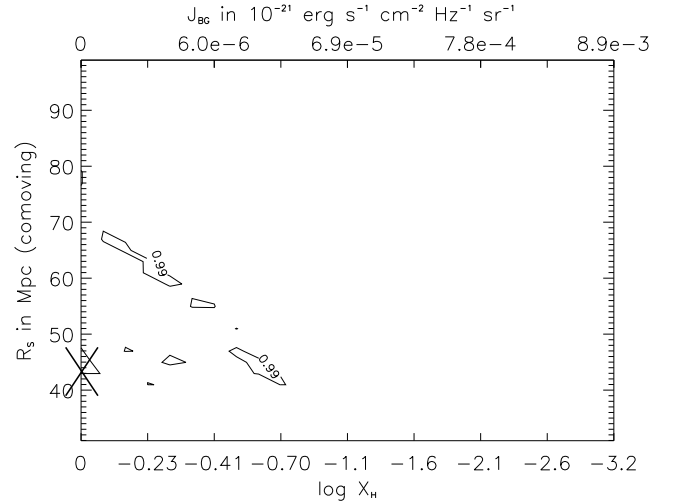


FIG. 5.— Probability contours for the inferred neutral fraction and Strömgen sphere radius, generated by the analysis in § 3.1. The background IGM is assumed to be neutral, and the X marks the position of the true value of R_S and x_H . *Top panel:* The inversion procedure is applied to a single source. The 90% confidence contours (not shown) enclose only the true (x_H, R_S) values, to within an error of (30%, 5%), respectively (only the single pixel containing the correct (fiducial) values is enclosed within these contours). Confidence contours of 99% are shown, and constrain the IGM neutral fraction to $x_H \sim 0.1$. The irregular, island shaped contours are the result of the unique features of a single LOS. *Bottom panel:* Probability contours generated by averaging the same analysis over five random LOSs (averaging χ^2 values from eq. [10]). The irregular, 99% confidence peaks from the *top panel* are smoothed out, and the contours are tighter. The correct (x_H, R_S) values were chosen with 99% confidence, to within an error of (30%, 5%), respectively (contour not shown). The 99.73% and 99.99% contours (solid and dashed lines, respectively) are shown, ruling out a $x_H \sim 0.1$ universe at better than 4 σ significance.

The results of this procedure can be seen in Figures 5 and 6, and are quite encouraging. These figures show likelihood contours for combinations of (x_H^0, R_S^0) for two cases of the true parameters, $(x_H, R_S) = (1, 43 \text{ Mpc})$ and $(x_H, R_S) = (0.008, 43 \text{ Mpc})$. The statistical constraints shown in these figures are obtained from one typical LOS to a single source. Both cases had a minimum reduced $\chi^2 = 1$ for 22 degrees of freedom ($d \nu : f := (N_{\text{bins}} - 1) - 2$). The $x_H - R_S$ probability grid in Figures 5 and 6 consists of 25×35 grid points, respectively.

In the case of a neutral universe (top panel of Fig. 5), the correct values of (x_H, R_S) , to within an error of (30%, 5%), respectively, are identified by our procedure at 90% confidence. We do not display these contours, as they would be represented by a point in the figure. Confidence contours of 99% are shown, and constrain the IGM neutral fraction to $x_H \sim 0.1$. The irregular, island contours in the top panel of Fig. 5 are the result of the unique features of a single LOS, and get smoothed out when averaged over several LOSs, as seen in the bottom panel. The bottom panel of Figure 5 shows the probability contours, averaged over five different random LOSs. The correct (x_H, R_S) values were chosen with 99% confidence, to within an error of (30%, 5%), respectively. The 99.73% and 99.99% contours (solid and dashed lines, respectively) are shown, ruling out a $x_H \sim 0.1$ universe at better than 4 σ , and an $x_H \sim 0.7$ universe at 3 σ . As expected, confidence contours get tighter as more LOSs are analyzed.

For the case of an ionized universe with $x_H = 0.008$ in Fig. 6, the 1 σ uncertainty contours (not shown) enclose the correct parameters, but the contours obtained from the single LOS are not as tight as in the neutral universe case, as was predicted in the introduction. Nevertheless, a neutral universe was ruled out at the 99% confidence level, as shown in Figure 6.

It is worthwhile to note that the iso-contours in Figures 5 and 6 go from bottom right to top left, indicating a degeneracy between small x_H , small R_S , and large x_H , large R_S solutions. This is to be expected since the contribution of ν_D to the observed spectrum can be diminished both by moving the edge of the Strömgen sphere further away from the source (increasing R_S), or by having a more highly ionized IGM (decreasing x_H). Due to the limited spectral range used, the determination of the amplitude of the host's intrinsic emission, A^0 , is most affected by this degeneracy; however, since the shapes of the damping wings are different in these scenarios, the degeneracy is not exact and can be lifted by increasing the number of sources used in the analysis.

A useful by-product of this procedure is that it produces an estimate of the amplitude of the intrinsic emission ($A^0 = A$ for

the correct choice of (x_H, R_S)).

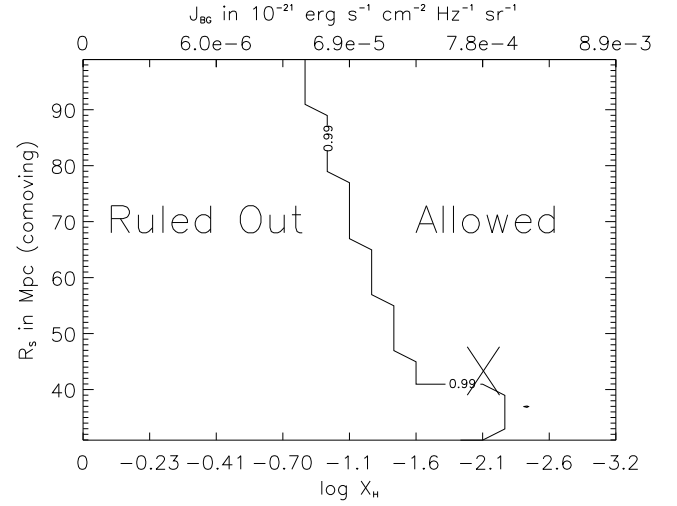


FIG. 6.— Probability contours for the inferred hydrogen neutral fraction and Strömgen sphere radius, generated by the analysis in § 3.1. The analysis is applied to a single source. The background IGM is assumed to have $x_H = 0.008$, and the X marks the position of the true value of R_S and x_H . Contours denote the 99% confidence limits, and rule out a neutral universe.

An interesting issue of biasing can be raised here. Since the quasar sits in an overdense region, histograms of R_S could have a rather large scatter close to the line center due to the increased spread in the density distributions and the peculiar motion of the gas within the infall region around the halo (e.g., Barkana & Loeb 2003). This biasing effect was studied, and on average, we find that the density field reaches within 15% of the mean density $\sim 5 \text{ Å}$ blueward from the observed line center, for our redshift $z_s = 6$ quasar. However, the distribution of densities at a fixed distance has a high-end tail, comprised of a few LOSs. Although we can model this bias for our quasar, one would need the density profiles surrounding many host sources to fully explore these statistics for a larger sample of quasars. This is feasible in principle, in large future simulations. However, for the purposes of generality, in the present paper the blue side of the spectra was cut-off 5 Å blueward of the line center and omitted from our analysis. Environment biasing will be discussed in detail in § 5.3.

Another uncertainty can arise if the redshift of the Ly α line center is not well determined. An offset in the line center of 1000 km s^{-1} (typical of quasar jets), results in an effective R_S offset of only ~ 1.3 comoving Mpc. A larger systematic offset of $z = 0.01 - 0.05$ in the line center, corresponding to $R_S = 4 - 20 \text{ Mpc}$, can be present if an associated metal line with a well-determined redshift has not been detected. This can represent a non-negligible misestimate in the radius of the ionized region (especially for faint sources), and underscores the importance of accurate redshift-determinations from metal-line detections. Nevertheless, we note that even these relatively large R_S uncertainties do not have a major impact in distinguishing among the x_H values of interest, which are separated by two orders of magnitude. This can be seen explicitly by noting that a vertical change of order $R_S = 4 - 20 \text{ Mpc}$ along the probability iso-contours, seen in Figures 5 and 6, corresponds to less than an order of magnitude change in the value of the neutral fraction. This is the case even for fainter sources, as discussed below.

4.2. Simulating Error in the Emission Template

The assumption of knowing the shape of the quasar’s intrinsic emission is not as outlandish as it might seem. Vanden Berk et al. (2001) created a composite quasar spectrum from 150 SDSS spectra of quasars around $z \approx 3$. Even though there were variations in amplitude, the normalized, mean template was defined around the Ly α line to better than 5%. Although spectrum-to-spectrum variations are considerable in the core of Ly α and blueward, most of these variations are accounted for by the Baldwin effect (the decrease of emission line width with increasing luminosity) and the absorption by the Ly α forest, both of which can be statistically removed. Hence, for this paper, we assumed spectrum-to-spectrum variations of $\sim 20\%$; a typical value of the r.m.s. scatter in the continuum level immediately redward of Ly α (Vanden Berk et al. 2001).

Fan et al. (2003) demonstrate that the high-redshift quasars follow Ly α emission line and continuum spectral shapes that are remarkably similar to that of their low-redshift counterparts. More precisely, the high redshift sample size is small, but the spectra of the present handful of $z \approx 6$ quasars are consistent with being drawn from the Vanden Berk et al. distribution of spectral shapes (Fan 2003, private communication).

Here we address the effect of the uncertainties of the assumed spectral template in two ways: we assume (1) an unknown overall “tilt” in the spectrum, or (2) an unknown pixel-to-pixel, uncorrelated, normally distributed scatter around a well-determined mean spectrum. These uncertainties add extra parameters in our analysis, and make the constraints on the neutral fraction less tight. However, as we will argue below, tight statistical constraints on the neutral fraction can still be obtained with a sufficiently large sample of high redshift sources.

4.2.1. Tilt in the Emission Template

The uncertainty in the emission template was first modeled with a pivoting procedure, chosen to be hinged at the wavelength used for the amplitude estimation in eq. (7), $\lambda_{\text{piv}} = \lambda_{\text{red}} = 8514 \text{ \AA}$. This mimics an incorrectly chosen power-law for the quasar’s continuum emission (and also a tilt in the Ly α emission line profile). Such a tilt would also characterize an uncertainty in the power-law index of GRB afterglow spectra (see § 5.2).

Thus, the observed flux is assumed to be of the form: $F(\lambda_{\text{obs}}) = A \left(\frac{\lambda_{\text{obs}}}{\lambda_{\text{piv}}} \right)^{-D} e^{-R(\lambda_{\text{obs}} - \lambda_{\text{D}})} e^{-R_S \lambda_{\text{H}}}$. Furthermore, equation (8) is modified to:

$$\hat{R}(\lambda_{\text{obs}}) = -\ln(e^{R(\lambda_{\text{obs}} - \lambda_{\text{D}})} e^{-\frac{A}{A^0} \left(\frac{\lambda_{\text{obs}}}{\lambda_{\text{piv}}} \right)^{-D}}) - \ln \frac{A}{A^0} - \frac{\lambda_{\text{obs}}}{\lambda_{\text{piv}}} \quad (11)$$

where λ_{piv} is now a guess for the spectral slope D .

The shape of this power-law tilt is similar, but not mathematically degenerate with the shape the damping wing. It therefore causes constraints to degrade. Here we characterize this degradation using:

$$hN_{\text{tilt}} \approx \frac{1}{2} \quad (12)$$

where hN_{tilt} is an estimate of the number of data points (i.e. spectral resolution bins) required to distinguish between the two spectrum shapes, and $hN_{\text{tilt}} = \frac{D - D_{\text{tilt}}}{D_{\text{tilt}}}$, with $D_{\text{tilt}} = \frac{D - D_{\text{tilt}}}{D_{\text{tilt}}}$ being a measurement of the typical spread of the estimated D obtained from differences in the

shape of the power-law and the shape of the damping wing flux decrement, and $\Delta R = 0.1$ is the width of the template R histogram.

We find that the tilt in the emission template obtained with a misestimate of D is not degenerate with the shape of the damping wing for our quasar. The largest value of hN_{tilt} , obtained from our parameter space occurred for the degeneracy between the fiducial values of ($x_H = 0.008$, $R_S = 43 \text{ Mpc}$) and the parameter choice of ($x_H^0 = 1$, $R_S^0 = 99 \text{ Mpc}$) with a tilt misestimate of $D - D_{\text{tilt}} = -3$. For these values, $hN_{\text{tilt}} \approx 10^3$, corresponding to, e.g., 10 similar quasar spectra with 100 usable independent spectral resolution elements.

4.2.2. Pixel-by-Pixel Errors

The uncertainty in the emission template was next modeled assuming uncorrelated, Gaussian distributed errors. Such pixel-by-pixel uncertainties could also represent the noise associated with the flux detection in each bin. Hence, the value of the emission template, $T(\lambda_{\text{obs}})$, in the input flux in equation (6), now becomes a Gaussian distributed random variable with a mean value for each wavelength given by $hT(\lambda_{\text{obs}})$. The inversion equation to replace equation (8) then becomes:

$$\hat{R}(\lambda_{\text{obs}}) = -\ln(e^{R(\lambda_{\text{obs}} - \lambda_{\text{D}})} e^{-\frac{A}{A^0}}) - \ln \frac{A}{A^0} - \ln \frac{T(\lambda_{\text{obs}})}{hT(\lambda_{\text{obs}})} \quad (13)$$

In the case of small deviations from the template value, $\frac{T(\lambda_{\text{obs}})}{hT(\lambda_{\text{obs}})}$, $\hat{R}(\lambda_{\text{obs}})$ is approximately Gaussian distributed around $[-\ln(e^{R(\lambda_{\text{obs}} - \lambda_{\text{D}})} e^{-\frac{A}{A^0}}) - \ln \frac{A}{A^0}]$. The exact shape of the probability distribution of R resulting from the Gaussian uncertainty in $T(\lambda_{\text{obs}})$ was calculated and convolved with the template R distribution (top left panel in Fig. 4). This new, normalized, template histogram was used as the new probability density function, f_i , in the χ^2 statistic shown in (10).

To test the robustness of our results to these pixel-by-pixel errors, a random LOS was drawn from our pool of LOSs, a Gaussian distributed emission template, $T(\lambda_{\text{obs}})$, was generated to create the mock spectrum, and the inversion procedure outlined in § 4.1 was performed, using equation (13) to generate the R histograms. This procedure was repeated, updating the χ^2 values in the parameter space with each newly processed LOS (each new LOS representing a different source in a hypothetical sample) until we were able to distinguish a neutral universe from a $x_H < 0.008$ universe with 99% confidence.

The results for the number of sources needed for the 99% confidence constraints are summarized in Table 1. The emission uncertainties refer to the standard deviation of the pixel-by-pixel Gaussian distributed errors in the emission template. With a 20% uncertainty in the intrinsic emission template, an average of, $hN_{\text{LOS}} \approx 34$ LOSs were required to rule out a neutral universe when the true value of the hydrogen neutral fraction was $x_H = 0.008$. In the $x_H = 1$ regime, only ≈ 3 spectra on average were required to rule out a $x_H < 0.008$ universe with 99% confidence. This should be expected, since as discussed previously, the neutral IGM leaves a heavier footprint on the quasar spectra for a reasonably sized Strömgen sphere.

Aside from the implicitly assumed calibration and elimination of the Baldwin effect, the adopted 20% uncertainty does not make use of any information (such as correlations with other observables) from the observed spectrum being processed

to further improve constraints. Preliminary results from a principal component analysis (PCA) of the spectrum-to-spectrum variations suggest that one might be able to characterize the variance in the emission template with only three eigenvalues (Vanden Berk 2003, private communication). It is likely that with such characterization of the variance and the usage of information redward of Ly α , the template uncertainty can be reduced, thus reducing $\ln N_{\text{LOS}}$. With a 10% pixel-by-pixel uncertainty, an average of 25 LOSs were needed to rule out a neutral universe for $x_H = 0.008$, and 3 to rule out an $x_H < 0.008$ universe for $x_H = 1$. A 5% uncertainty brings the average number of required spectra down to 14 and 2, for $x_H = 0.008$ and $x_H = 1$, respectively. These results, as well as the r.m.s. deviations, are summarized in Table 1.

TABLE 1
AVERAGE NUMBER OF BRIGHT QUASARS REQUIRED TO
DISTINGUISH BETWEEN $x_H = 1$ AND $x_H < 0.008$ WITH 99%
CONFIDENCE.

Emission Uncertainty	$\ln N_{\text{LOS}}$ with $x_H = 1$		$\ln N_{\text{LOS}}$ with $x_H = 0.008$	
20%	3.42	1.95	33.6	20.8
10%	3.39	2.15	24.6	20.0
5%	2.45	1.13	16.8	14.2

5. MERITS OF DIFFERENT SOURCE TYPES

Although the preceding analysis was done with simulated quasar spectra similar to the bright SDSS high-redshift quasars, it can be repeated on other high-redshift sources, namely quasars with lower luminosities, high-redshift galaxies and GRB afterglows. The properties of the sources scale predictably with their luminosities, with the two most pertinent to this analysis being the size of the source's Strömgren sphere and the shape of the source's intrinsic emission spectrum.

5.1. Strömgren Sphere Size

The size of the source's Strömgren sphere, R_S , approximately scales as the source's (luminosity) $^{1/3}$. A fainter quasar, of similar age, might therefore have fewer measurable spectral points inside the Strömgren sphere, with which to create the $\ln N_{\text{LOS}}$ histogram, which weakens constraints. On the other hand, since the Strömgren sphere is smaller, the damping wing has a stronger effect on the spectrum, which strengthens constraints.

To estimate the overall effect on the determination of the neutral fraction, we repeated the pixel-by-pixel analysis outlined in § 4.2.2 on a 100 times fainter quasar ($L = 2.34 \times 10^{29} \text{ erg s}^{-1} \text{ (} x_H = 1 \text{)}^{0.8} [(1+z)=(1+z_S)]^{0.8}$) with a correspondingly smaller Strömgren sphere ($R_S = 9.3 \text{ Mpc}$). From simulated spectra of such mock quasars in a neutral universe, we find that a $x_H < 0.008$ universe is ruled out at 99% confidence with ~ 3 LOSs. This result is therefore comparable to that available from the brighter quasars (shown in Table 1). This can be understood by realizing that even though fewer spectral points are available for the analysis of a fainter source (since the Strömgren sphere is smaller), these points are those close to the edge of the Strömgren sphere where the damping wing has a sharper slope, and are given more statistical weight due to the lack of

points far away from the edge of the Strömgren sphere, where the damping wing is flatter. On the other hand, we find that approximately $10^2 - 10^3$ faint quasar LOSs are needed on average, for the emission template uncertainties of 5%-20%, in order to break the degeneracy between the damping wing of a small x_H , small R_S and a large x_H , large R_S parameter choice. Since the probability iso-contours go from bottom right to top left in the parameter space of Figure 5, limiting parameter space to $R_S < 100 \text{ Mpc}$ (as we had implicitly done above) allowed for a stronger degeneracy in an ionized universe in the case of a small R_S than in the case of the larger R_S quasar used throughout the preceding analysis in this paper. If instead we limit parameter space to $R_S < 30 \text{ Mpc}$, the fainter sources are able to distinguish between a neutral universe and a $x_H < 0.008$ universe, using again a comparable number (i.e., tens) of sources to the brighter quasars shown in Table 1. Whether limiting the size of the Strömgren sphere to 30 Mpc is a reasonable prior assumption depends on the actual inferred neutral fraction. The size of the Strömgren sphere scales as $x_H^{-1/3}$, and for sources that are ~ 100 times fainter than the $z = 6$ SDSS quasars, they would require $> 10^7$ years to reach a 30 Mpc size even if embedded in an IGM with neutral fractions as low as $x_H = 0.008$.

An implicit drawback of fainter sources is that they have smaller S/N than bright sources, thereby reducing the effective detection threshold. Becker et al. (2001) and White et al. (2003) state the 1 σ lower limits to the Ly α optical depth inferred from the Ly α trough to be $\lim_{\tau} \sim 5$ or 6, for the Keck ESI spectra of $z = 6$ quasars. As stated previously, the analysis in this paper ignored inferred values of $\tau > 16$. Because of the sharp drop in the high-end tail of the τ histograms (see Fig. 4), the inversion procedure presented in § 4.1 is not sensitive to the exact value of the detection limit. In our template histogram, only 5% of the values were within the range $6 < \tau < 16$, approximately corresponding to data points used in the analysis, which are undetectable with $\lim_{\tau} \sim 6^3$. However, a 100 times fainter quasar would have its optical depth detection threshold reduced by $\ln(100)=4.6$ to obtain equivalent S/N for the same integration time. For our mock spectra, this would eliminate an additional 20% of the τ values, in the range of $1.4 < \tau < 6$. Hence, fainter sources have a smaller range of usable τ values than brighter sources. Nevertheless, higher S/N observations would decrease this effect.

Sources that are too faint to have many detectable spectral points on the blue side of the line, such as faint galaxies and GRB afterglows, would not be useful in this τ histogram analysis, but would still have a strong damping wing imprint on their spectrum redward of Ly α . As mentioned previously, redward of Ly α , τ is negligible, and the small-scale power analysis presented in § 4.1 is irrelevant. If the sources are intrinsically faint enough, the slope of the damping wing redward of Ly α is sufficient to distinguish between a small R_S , small x_H case and a large R_S , large x_H scenario with only a few sources. As emphasized recently by Lamb & Haiman (2002) and Barkana & Loeb (2004), GRB afterglows with a clean power-law intrinsic spectrum would be especially well suited to such an analysis, provided they can be identified in future datasets (e.g. of Swift).

As an example, the usefulness of the red side of the Ly α line in determining x_H was also investigated for our simulated faint quasar with $R_S = 9.3$ and $x_H = 0.008$, assuming pixel-to-pixel

³There is a small bias associated with the fact that the detection limit, \lim_{τ} , is a limit on the total optical depth, $\tau_{\text{tot}} = \tau + \tau_D$, and not just τ .

Gaussian scatter in the emission template. In principle, sufficiently far on the red side of the Ly α line, where resonant absorption does not contribute, this analysis could be performed without a numerical simulation. However, due to the cosmic infall, some of the pixels immediately on the red side of the Ly α line center correspond to foreground gas between us and the quasar (the resonant absorption extends, in our case, up to 7-8 Angstroms to the red, see Figure 8). For this reason, we did use the simulation in the analysis. Alternatively, to avoid uncertainties due to modeling the cosmological infall, one could omit the spectral regions that are blueward of the infall regime. Here we utilized the flux in the observed wavelength range of 8514 Å – 8544 Å and performed a simple comparison. A more robust analysis of the red side would involve χ^2 minimization in the 3-dimensional parameter space of (x_H, R_S, A) , where A is the amplitude of the intrinsic emission. However, for purposes of comparison to the R histogram analysis presented in § 4.1, it was sufficient to obtain an estimate of A using an assumed region in the observed spectrum with an accurately known template shape, and calculating A^0 as outlined in § 3.1 and equation (7). For a choice of x_H^0 and R_S^0 , we therefore obtain an estimate of the flux decrement due to resonance absorption, $d_R(\lambda_{\text{obs}}) = F(\lambda_{\text{obs}}) \frac{e^{-\frac{\lambda_{\text{obs}} - \lambda_0}{\Delta\lambda}}}{A^0 h T(\lambda_{\text{obs}})}$, which expands to:

$$d_R(\lambda_{\text{obs}}) = e^{-R(\lambda_{\text{obs}})} \frac{A}{A^0} \frac{T(\lambda_{\text{obs}})}{h T(\lambda_{\text{obs}})} e^{\frac{\lambda_{\text{obs}} - \lambda_0}{\Delta\lambda}} \quad (14)$$

For the correct parameter choices, $d_R(\lambda_{\text{obs}}) \approx e^{-R(\lambda_{\text{obs}})}$, since $R \neq 0$ on the red side of the line and redward of the infall regime. The mean flux decrement, $\langle d_R(\lambda_{\text{obs}}) \rangle$, averaged over several randomly chosen LOSs, was compared to the average decrement obtained from the simulated spectra at each wavelength, $\langle e^{-R(\lambda_{\text{obs}})} \rangle$, with the χ^2_R statistic:

$$\chi^2_R = \frac{\sum_{l_{\min}}^{l_{\max}} (\langle e^{-R(\lambda_{\text{obs}})} \rangle - \langle d_R(\lambda_{\text{obs}}) \rangle)^2}{\frac{2}{m}} \quad (15)$$

where the summation limits were chosen to be $l_{\min} = 8514$ Å and $l_{\max} = 8544$ Å and m is the standard deviation of the intrinsic emission template divided by the square root of the number of LOSs used in determining the mean decrement, $\langle d_R(\lambda_{\text{obs}}) \rangle$. LOSs were chosen at random, and the mean decrement and test statistic in equation (15) were updated until a neutral universe could be ruled out at 99% confidence.

Results from this procedure are quite comparable to the R histogram analysis on the blue side of the Ly α line for our faint quasar with $R_S = 9.3$ and $x_H = 0.008$. On average, we find that $10^2 - 10^3$ LOSs were needed to rule out a neutral universe at 99% confidence for template uncertainties of 5%-10%, just as in the R histogram analysis. Although the red side is cleaner (negligible resonant absorption), it is further away from the edge of the Strömgren sphere, so the damping wing shape is flatter and is therefore harder to detect. However, our results suggests that if a larger wavelength range is available for the analysis, or if the source has a smaller Strömgren sphere (a few Mpc), analyzing the red side of the Ly α line could prove more efficient than the blue side in determining x_H .⁴

⁴There is an additional complication that an intervening damped Lyman alpha (DLA) system along the line of sight causes absorption whose shape is partially degenerate with that due to the damping wing from a smooth IGM (Miralda-Escudé 1998; Barkana & Loeb 2004). However, the degeneracy is not exact, and lines of sight with DLAs should be rare.

Furthermore, very faint sources have other tracers of x_H . For example, Haiman (2002) showed that the shift in the peak of the observed Ly α emission line (relative to other emission lines), or its measured asymmetry, as a function of the source luminosity, can be used as a probe of the IGM hydrogen neutral fraction.

5.2. Intrinsic Emission

Our knowledge of the source's intrinsic emission varies considerably with source type. Again, it is only the imperfect knowledge of the shape of the emission spectrum that complicates the analysis presented here (i.e. knowledge of the overall amplitude of the spectrum is not needed). On average, quasars seem to have a moderately well constrained emission template around Ly α , with an uncertainty of $\sim 20\%$, once the spectrum is normalized and systematics such as the Baldwin effect are accounted for. It is possible that this uncertainty could be further decreased with a principal component analysis (PCA), which has yielded well-characterized spectrum-to-spectrum dispersions on the red side of the Ly α line (Vanden Berk 2003, private communication). In comparison, the spectral shape of emission from galaxies is more poorly defined around Ly α (Steidel et al. 2001). One would therefore need larger samples of Ly emitting galaxies at both lower redshifts and higher redshifts for a better empirical calibration of their spectral shape and its dispersion. Such samples may soon be available from extensive Ly α searches using HST (Rhoads et al. 2003) and Subaru (Taniguchi 2003). GRB afterglows have a smooth power-law spectrum shape. There appears to be a scatter in the power-law index of roughly $\sim 10\%$ in photometric data on low-redshift bursts. The sample of higher-redshift bursts, whose spectral shape can be studied in more detail around the Ly α line, is still too small to quantify spectrum-to-spectrum dispersions, but they appear to closely follow power-laws (Mirabal et al. 2003). Note that a pure power-law uncertainty is not degenerate with the shape of the damping wing (see § 4.2.1). The major issue with GRB afterglows will be whether the high-redshift afterglows can be identified among the lower-redshift events (see, e.g., Lamb & Reichart 2000 and Barkana & Loeb 2004 for recent discussions).

5.3. Environment Bias

The source's host environment has a large effect on the observed spectrum near the line center, as emphasized recently by Barkana & Loeb (2004). To accurately model this effect, and to test semi-analytical models (Barkana 2004) hydrodynamical simulations are needed to generate the local density and velocity fields. In Figures 7 and 8, we show the effect of this biasing for our mock quasar. Figure 7 shows the histograms of the spherically averaged (within our set of 92 lines) radial component of the peculiar velocity fields constructed from 2 Å bins in λ_{obs} , at increasing distances away from the quasar. Most of the radial velocities closest to the host pixel exhibit strong infall, with the PDF peaking at peculiar radial velocities of $v \sim -100$ km/s. However, there is a significant, high-velocity tail in the distribution, corresponding to several LOSs that exhibit strong outflows (100-500 km/s) close to the host pixel. As the distance from the central overdensity increases, the radial velocity PDFs become narrower and more centered around 0 km/s, as is expected for a randomly chosen point in space. Strong outflow features disappear ~ 5 Å away from the line center. After about 10 Å away from the line center, the velocity histogram becomes quite symmetric around 0 km/s.

These proximity effects have a strong impact on the resonance optical depth, τ_R , as shown in Figure 8. The dotted curve shows τ_R calculated assuming the mean density, $n_H(z) = n_{H0} (1+z)^3$, and not including velocity information from the simulation. The dashed curve includes the density field from the simulation, but not the velocity field. Finally, the solid curve includes both the density and velocity information from the simulation box. The values of τ_R shown in this figure were averaged over all LOSs: $-\ln e^{-\tau_R}$. The figure clearly shows that the peculiar velocities around the density peak smooth out the spectrum, and create a more gradual decline in the optical depth redward of $\text{Ly}\alpha$. Overdensities close to the line center become regions of relatively low optical depth, since the gas Doppler shifts out of resonance. Further away on the blue side from the host overdensity, the scatter in the density and velocity fields among different LOSs decreases, and the velocity histogram becomes centered around 0 km/s (as mentioned above), so the difference between the averaged τ_R curves becomes statistically negligible.

These figures merely emphasize that density biasing due to the host environment is important, and it requires a larger simulation with a statistical sample of density peaks to quantify. We plan to carry out such an analysis in detail in a future paper. In particular, the analysis presented in this paper should be performed for a larger number of density peaks in other simulation boxes for the density bias to be statistically analyzed. In actual data analysis, it should help that the host environment should scale with the halo size, and therefore with the source's luminosity.

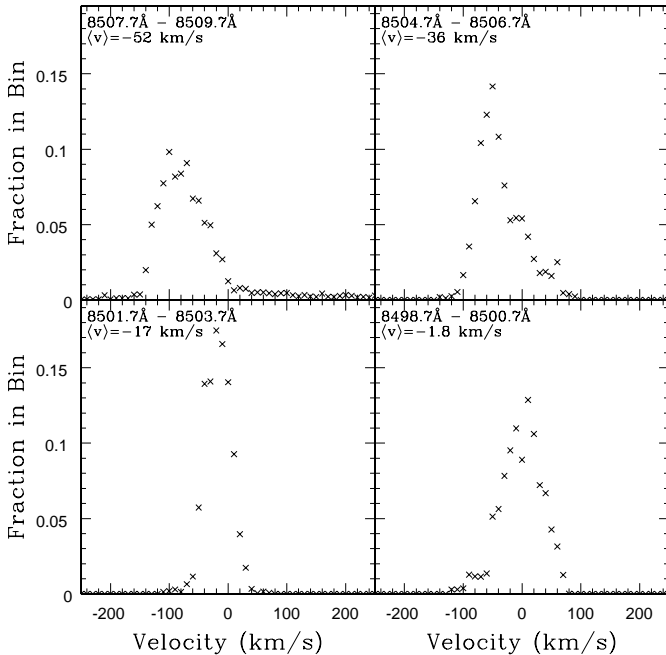


FIG. 7.— Spherically averaged radial velocity histograms at several distances, corresponding to redshifts of $z = z_{\text{obs}} - 1$, away from the host pixel at $z_s = 6$. The histograms are constructed from different λ_{obs} ranges: 8507.69 Å - 8509.69 Å (top left), 8504.69 Å - 8506.69 Å (top right), 8501.69 Å - 8503.69 Å (bottom left), and 8498.69 Å - 8500.69 Å (bottom right). The fraction of infalling gas decreases with increasing distance from the central overdensity, until at about 10 Å away from the line center, at which distance the histogram becomes nearly symmetric around 0 km/s. Close to the central overdensity (top left), most of the gas has large negative radial velocities, but there is a significant, high-velocity tail in the distribution.

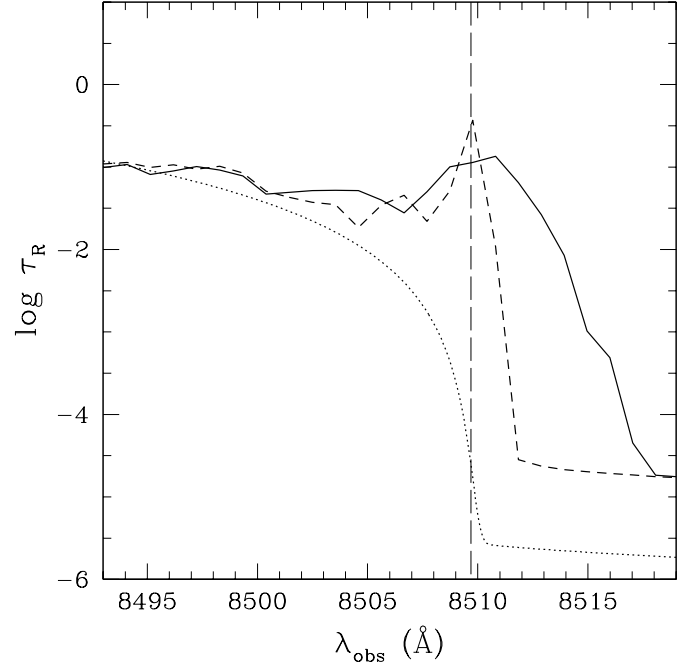


FIG. 8.— Values of τ_R averaged over all LOSs: $-\ln e^{-\tau_R}$. The dotted curve shows τ_R calculated assuming the mean IGM density, $n_H(z) = n_{H0} (1+z)^3$, and not including velocity information. The dashed curve includes the density field from the simulation, but not the velocity field. The solid curve includes both the density and velocity information from the simulation box. The long dashed vertical line denotes the $\text{Ly}\alpha$ line center at 8509.69 Å. The solid curve can be approximately reproduced by convolving the dashed curve with the velocity PDFs at each λ_{obs} . Including velocity information smooths out the spectrum, and creates a more gradual decline in the optical depth redward of $\text{Ly}\alpha$. Further away on the blue side from the host overdensity, the difference between the averaged τ_R curves becomes statistically negligible.

On the other hand, the biased region does not encompass the majority of the spectrum, as mentioned in § 4.1. For our mock quasar, the biased region extends only ~ 5 Å away from the line center. However, since our halo is smaller than that expected to host typical $z \sim 6$ quasars, the biased region could be larger for a more realistic, more massive halo. Using a semi-analytical model, Barkana & Loeb (2004) recently derived the gas density and velocity distributions around the relevant halos. They find (see their Figure 1) that for halo masses typical of those expected to host the bright SDSS quasars, the biased region should extend about ~ 1 Mpc (proper). This translates to a wavelength range of ~ 20 Å and still influences less than 1/6 of the region used in our analysis. Our initial results therefore suggest that one can extract τ_R^0 histograms from spectra even without modeling the density bias, by ignoring this part of the spectrum around the line center, as was done in this paper.

It is interesting to ask which part of the optical depth distribution carries the most statistical power - the low, or the high-optical depth pixels, since the low-optical depth pixels are preferentially effected by biasing effects. We addressed this issue by computing the statistical power of fractions of our τ_R histograms. We found that similar constraints are obtained by using only pixels with $\tau_R < 0.1$ and by using only pixels with $\tau_R > 0.1$ (see Fig. 4). Approximately 1/3 of the underdense ($\tau_R < 0.1$) pixels used in our analysis are expected to lie within the biased region discussed above. It would clearly be beneficial to have accurate statistics of the biasing of host halos, but this is impractical given current computational constraints. The

simplest way to deal with the issue is to remove the biased region from the analysis (as was attempted in this paper). Since the majority of pixels are not affected, as discussed above, we expect our results to be fairly insensitive to biasing.

As a final test of local bias, we created a new template distribution of τ_R values by using LOSs generated from a new and independent simulation box. The densest region in the new box, from which LOSs originated, corresponds to a dark matter halo of mass $M_{\text{halo}} = 1 \times 10^{10} M_\odot$, about 1/2 the mass of the densest halo in the simulation box used throughout the rest of this paper. The two template distributions can be seen in Fig. 9, with *squares* representing the new histogram, and *crosses* showing the old histogram (i.e. the top left panel of Figure 4). The two histograms are fairly similar (their difference is much smaller than those between the models being compared to one another in Figure 4). Our old template is somewhat wider, as would be expected from the larger density contrast we find in that simulation box. The density field around the new halo reaches within 15% of the mean density $\sim 5 \text{ \AA}$ blueward from the line center, just as in the former halo.

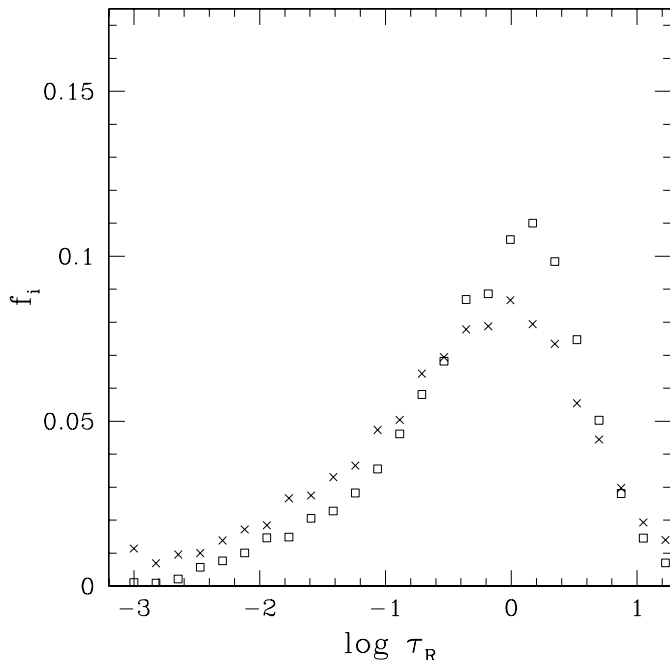


FIG. 9.— Histogram of the template distribution of τ_R from LOSs originating at a dark matter halo of mass $M_{\text{halo}} = 2 \times 10^{10} M_\odot$ (*crosses*), and originating at a dark matter halo of mass $M_{\text{halo}} = 1 \times 10^{10} M_\odot$ (*squares*). The former distribution was used throughout this paper. The later distribution was created from a different simulation box, in order to investigate uncertainties in the template. The two distributions are similar, with the histogram corresponding to a larger mass host halo being somewhat wider due to the larger density contrast in the simulation box.

6. ADDING ADDITIONAL CONSTRAINTS: LIMITS ON R_S

As discussed above, the dominant factor in this analysis is the degeneracy between small x_H , small R_S , and large x_H , large R_S parameter choices. Hence, it would be quite useful to be able to independently restrict allowed values of R_S . This is difficult since the mean resonant optical depth grows roughly as the square of the distance away from the source, so resonance absorption inside the Strömgen sphere can be sufficient to block out Ly α flux alone, especially considering uncertainties in the

source’s ionizing luminosity.

However, a particularly important piece of information that we have not utilized in this paper is that the R_S histograms could be constructed as a function of λ_{obs} , instead of lumping them into a single histogram regardless of wavelength. In general, if a large number of spectra were available, this would contain more information, and would help characterize density biases, which should be a strong function of distance away from the source.

More specifically, however, Mesinger & Haiman (2004) (hereafter, MH04) recently presented a method, which takes only a crude account of the wavelength–dependence of the opacity, using essentially only the location of the Ly α and Ly β GP troughs, to find a robust determination of R_S . Since the different hydrogen Lyman transitions have disparate oscillator strengths, simultaneously considering the measured absorption in two or more Lyman lines can be an effective way to probe a sudden growth of the Ly α optical depth near the boundary of the Strömgen sphere. In MH04, we applied this technique to model the general behavior of the observed spectrum of SDSS J1030+0524 close to the onset of the Ly α and Ly β GP troughs. We obtained a tight and robust constraint on R_S (better than 5%), arising from the sharpness of growth of the Ly α optical depth. If this (or any other) method can be used to independently constrain R_S to within $\sim 10\%$, it would break the degeneracy between small x_H , small R_S , and large x_H , large R_S parameter choices. Specifically, if R_S is known to within $\sim 10\%$, a neutral universe could be distinguished from a $x_H < 0.008$ universe with 99% confidence using an average of only 1 source, following the method presented in this paper (note that an independent constraint on the neutral fraction can be derived from the size of the HII region, by utilizing the estimated ionizing flux of the source; Wyithe & Loeb 2004). The usefulness of knowing R_S can be seen from Figure 2, where all panels have the same R_S and there is a large difference between the flux decrements arising from a neutral (*left panels*) and an ionized (*right panels*) IGM. This is a highly encouraging result, and we plan to apply both the method in MH04 and the method presented in this paper to the current sample of SDSS quasars.

7. CONCLUSIONS

Through an analysis of mock quasar absorption spectra based on a detailed cosmological hydrodynamic simulation, we have shown that it is possible to detect the effects of the damping wing of absorption by neutral hydrogen atoms in the IGM on top of the resonant absorption from within the local HII region of the quasar. We have described an inversion method we have developed to extract an estimate of the mean neutral fraction of hydrogen in the IGM, and of the size of the Strömgen sphere around a high-redshift source. The method is designed to differentiate between sources embedded in an IGM with $10^{-3} < x_H < 1$, and we have found that it can distinguish among neutral fractions in this range with only a few bright quasars.

We have explicitly incorporated into our analysis an error in the intrinsic emission template, consisting of either an uncertainty in its spectral power-law index, or Gaussian, uncorrelated, pixel-to-pixel variations at each wavelength. With both of these errors, we find that a neutral universe can be statistically distinguished from a $x_H = 0.008$ universe in our parameter space, using tens of bright quasars, a sample that can be expected by the completion of the Sloan Digital Sky Survey. Al-

ternatively, similar statistical constraints can be derived from the spectra of several hundred sources that are 100 times fainter. For example, the Large-aperture Synoptic Survey Telescope (LSST) should be able to deliver many new faint quasars that could serve as targets for low-resolution spectroscopy (Mesinger et al. 2004, in preparation).

Furthermore, if the size of the source's Strömgren sphere can be independently constrained to within 10% (such as with the method presented in MH04), the analysis presented here can distinguish between sources embedded in an IGM with $10^{-3} < x_H < 1$, using a single source. We plan to perform such analysis on the current sample of high-redshift sources.

The recent discovery of Gunn-Peterson troughs in the spectra of several $z \sim 6$ quasars in the SDSS only impose the restriction of $10^{-3} < x_H < 1$ on the neutral fraction at this redshift. Further distinguishing between the values allowed in this range, especially between a neutral and a mostly ionized universe, would provide invaluable new constraints that can differentiate among various competing reionization scenarios.

We thank an anonymous referee for a thorough and helpful report. Zoltán Haiman gratefully acknowledges support by the National Science Foundation through grants AST-0307291 and AST-0307200 and by NASA through grant HST-GO-09793.18. Renyue Cen thankfully acknowledges grants AST-0206299 and NAG5-13381.

REFERENCES

- Barkana, R. 2004, MNRAS, 347, 59
 Barkana, R., & Loeb, A. 2003, Nature, 421, 341
 Barkana, R., & Loeb, A. 2004, ApJ, 601, 64
 Becker, R.H., et al. 2001, AJ, 122, 2850
 Bennett, C.L., et al. 2003, ApJS, 148, 1
 Cen, R., et al. 1994, ApJ, 437, L9
 Cen, R. & Haiman, Z. 2000, ApJ, 542, L75
 Cen, R. & McDonald, P. 2002, ApJ, 570, 457
 Cen, R. 2003a, ApJ, 591, 12
 Cen, R. 2003b, ApJ, 591, L5
 Elvis, M., et al. 1994, ApJS, 95, 1
 Fan, X., et al. 2002, AJ, 123, 1247
 Fan, X., et al. 2003, AJ, 125, 1649
 Gnedin, N.Y. 2000, ApJ, 542, 535
 Haiman, Z., 2002, ApJ, 576, L1
 Haiman, Z., & Holder, G.P. 2003, ApJ, 595, 1
 Hansen, S.H., & Haiman, Z. 2003, ApJ, in press, astro-ph/0305126
 Kogut, A. 2003, ApJS, 148, 161
 Lamb, D., & Haiman, Z. 2002, in the proceedings of the 3rd Rome Workshop on Gamma-Ray Bursts in the Afterglow Era, held in Rome, September 2002, eds. L. Piro, F. Frontera, N. Masetti and M. Feroci, ASP Conf. Series, in press, astro-ph/0312502
 Lidz, A., Hui, L., Zaldarriaga, M. & Scoccimarro, R. 2002, ApJ, 579, 491
 Madau, P., & Rees, M.J. 2000, ApJ, 542, L69
 Madau, P., et al. 2003, ApJ, submitted, astro-ph/0310223
 Mesinger, A., & Haiman, Z. 2004, ApJL, submitted, astro-ph/0406188 (MH04)
 Mirabal, N., et al. 2003, ApJ, 595, 935
 Miralda-Escudé, J. 1998, ApJ, 501, 15
 Oh, S.P. 2001, ApJ, 553, 499
 Peebles, P.J.E. 1993, Principles of Physical Cosmology (Princeton: Princeton Univ. Press)
 Pentericci, L., et al. 2002, AJ, 123, 2151
 Rhoads, J. E., et al. 2002, BAAS, 34, 1195
 Ricotti, M., & Ostriker, J.P. 2003, MNRAS, submitted, astro-ph/0311003
 Rybicki, G.B., & Lightman, A.P. 1979, Radiative Processes in Astrophysics (New York: John Wiley & Sons)
 Songaila, A., & Cowie, L. L. 2002, AJ, 123, 2183
 Spergel, D.N. et al. 2003, ApJS, 148, 175
 Steidel, C.C., Pettini, M., & Adelberger K.L. 2001, ApJ, 546, 665
 Taniguchi, Y. 2003, in the Proceedings of the ESO/USM/MPE Workshop on "Multiwavelength Mapping of Galaxy Formation and Evolution", preprint astro-ph/0312228
 Vanden Berk et al. 2001, AJ, 122, 549
 Venkatesan, A., Giroux, M.L., & Shull, J.M. 2001, ApJ, 563, 1
 White, R. L., Becker, R. H., Fan, X., & Strauss, M. A. 2003, AJ, 126, 1
 Wyithe, J. S. B., & Loeb, A. 2003a, ApJ, 586, 693
 Wyithe, J. S. B., & Loeb, A. 2003b, ApJ, 588, L69
 Wyithe, J. S. B., & Loeb, A. 2004, Nature, 427, 815